Earthquakes and Structures, *Vol. 17, No. 1 (2019) 101-113*
DOI: https://doi.org/10.12989/eas.2019.17.1.101

A substructure formulation for the earthquake -induced nonlinear structural pounding problem

Jianye Shi[a], Franz Bamer[*] and Bernd Markert[b]

Institute of General Mechanics, RWTH Aachen University, Templergraben 64, 52064 Aachen, Germany

(Received June 12, 2018, Revised April 25, 2019, Accepted June 15, 2019)

Abstract. Earthquake-induced pounding is one of the major reasons for structural failure in earthquake prone cities. An accurate description of the pounding phenomenon of two buildings requires the consideration of systems with a large number of degrees of freedom including adequate contact impact formulations. In this paper, firstly, a node to surface formulation for the realization of state-of-the-art pounding models for structural beam elements is presented. Secondly, a hierarchical substructure technique is introduced, which is adapted to the structural pounding problem. The numerical accuracy and efficiency of the method, especially for the contact forces, are verified on an academic example, applying four different impact elements. Error estimations are carried out and compared with the classical modal truncation method. It is demonstrated that the hierarchical substructure method is indeed able to significantly speed up the numeric integration procedure by preserving a required level of accuracy.

Keywords: pounding problem; substructure technique; model order reduction; Craig-Bampton method

1. Introduction

Reports on several earthquake events show that pounding between adjacent buildings is a major reason for damage or even collapse (Kasai and Maison 1997, Chase *et al*. 2014, Jankowski 2005, Ghandil and Aldaikh 2017). Therefore, extensive research has been focused on pounding mitigation (Barbato and Tubaldi 2013, Zargar *et al*. 2017, Jankowski and Mahmoud 2016, Aldaikh *et al*. 2015, Abdel Raheem 2014), risk assessment (Barbato and Tubaldi 2013, Tubaldi *et al*. 2016) and the development of phenomenological contact elements. The latter should enable a realistic description of the pounding phenomenon. Earlier models are energy-conserving. This includes the linear elastic and nonlinear elastic model, which follows Hertz's law (Davis 1992, Pantelides and Ma 1998, Chau *et al*. 2003, Mavronicola and Komodromos 2011, Chau and Wei 2001). The obvious disadvantage of these models is that they do not consider energy dissipation. Thus, a linear viscoelastic model was proposed in the literature (Anagnostopoulos 1992); however, abrupt jumps at the beginning and the end time instants of the collision time period are observed. Additionally, unwanted tensile forces occur at the end of the restitution time period. Consequently, two state-of-the-art pounding models have been proposed in the literature, whereby neither abrupt jumps with regard to the collision force nor tensile forces are observed during the end of the restitution time period. Firstly, this includes the Hertz-Damp model (Muthukumar and DesRoches 2006, Zhang *et al*. 2014, Ye *et al*. 2009), which consists of a nonlinear Hertz spring and a nonlinear damping term. Secondly, the nonlinear viscoelastic model was proposed by Jankowski (Jankowski 2005, 2006, 2009). In this model, a nonlinear spring and a nonlinear damping term are active in parallel during the approach time period, but only the nonlinear spring is active during the restitution time period (Bamer 2018, Bamer and Markert 2018).

Although the presentation of enhanced pounding elements is mostly done using simple multi degree of freedom systems with conform collision conditions (node-to-node formulation), there are several papers in the literature, which apply finite-element-discretized structures for the description of the pounding problem (Pantelides and Ma 1998, Efraimiadou *et al*. 2013a, b, Ghandil and Aldaikh 2017). However, the strategies of how to include the state-of-the-art pounding models for the discretized structures, is not sufficiently discussed. Additionally, the treatment of high-dimensional dynamic problems is time consuming. Especially, the computation of the impact force in every calculation time step demands a considerably high computational effort, as search algorithms must be applied within the discretization of the defined collision surfaces. Thus, physically motivated model order reduction techniques can constitute effective strategies to overcome this issue. Model order reduction strategies for nonlinear systems, using the proper orthogonal decomposition method, have intensively been advocated in various fields of engineering over the last decades, and lately they have also been applied to materially nonlinear structures subjected to transient excitation (Bamer and Bucher 2012, Bamer *et al*. 2017a, Komodromos 2007, Bamer and

∗Corresponding author, Ph.D.
E-mail: bamer@iam.rwth-aachen.de
[a]Ph.D. Student
E-mail: shi@iam.rwth-aachen.de
[b]Professor
E-mail: markert@iam.rwth-aachen.de

http://www.techno-press.com/journals/eas&subpage=7 ISSN: 2092-7614 (Print), 2092-7622 (Online)

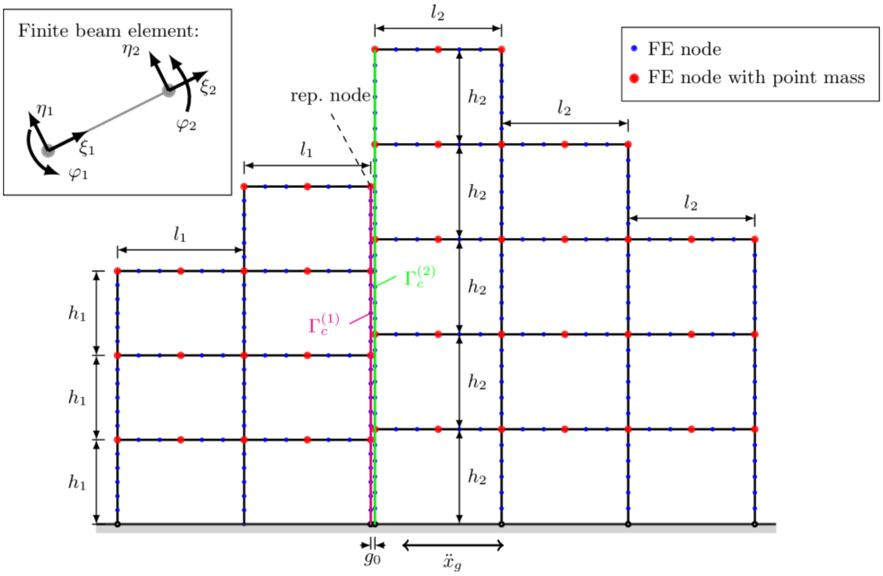

Fig. 1 Dynamic system of adjacent structures; finite beam element; frame height measures h_1, h_2; frame width measures l_1, l_2; initial gap g_0; slave ($\Gamma_c^{(1)}$) and master ($\Gamma_c^{(2)}$) contact surfaces and representative output node (rep. node)

Markert 2017). Regarding the efficient treatment of dynamic contact problems, the application of substructure techniques was proposed recently. In particular, a theoretical paper was published by Zucca and Epureanu (2017), who applied the Craig-Bampton (Craig and Bampton 1968) and the Dual Craig-Bampton method (Rixen 2004, Kim *et al*. 2017) to a multi-degree-of-freedom system with conform contact conditions. An enhanced Craig-Bampton method was proposed (Boo *et al*. 2018). The pounding force is also evaluated in the works of Kun *et al*. (2018), Kheyroddin *et al*. (2018), Bi *et al*. (2018). Additionally, the Craig-Bampton method was applied to efficiently solve the multiple pounding problem using linear impact elements within a node-to-surface formulation (Bamer *et al*. 2017b).

In this paper, an efficient hierarchical substructure technique is proposed and adapted to a node-to-surface formulation of state-of-the-art pounding models. Thus, within a step-by-step-procedure, the node-to-surface formulation of four different pounding models is introduced, and the applicability of the hierarchical substructure technique for this highly nonlinear type of problems is discussed. Firstly, in Section 2, the geometrical and material properties of the academic pounding problem, which goes along with the proposed strategy in the paper, is discussed. Subsequently, in Section 3, four applied pounding formulations for the node-to-surface collision are presented. Hereby, we discuss the simple energy-conserving linear and nonlinear Hertz model (Davis 1992, Pantelides and Ma 1998, Chau *et al*. 2003, Chau and Wei 2001); the Hertz-Damp model (Muthukumar and DesRoches 2006, Ye *et al*. 2009) and the nonlinear viscoelastic model (Jankowski 2005, 2006, 2009). In Section 4, the hierarchical Craig-Bampton strategy, adapted to structural pounding problems, is discussed. In Section 5, the numerical demonstration of the strategy, using the state-of-the-art pounding models, is presented, and, finally, in Section 6, the conclusion is drawn.

2. Academic structural pounding benchmark

In this section, an academic pounding example, used for the demonstrations in this paper, is presented. Two planar adjacent frame structures, as depicted in Fig. 1, are selected to represent the pounding benchmark example. As shown in this figure, the frames are arranged with an initial gap of $g_0 = 0.2$ m. The width and the height of the two frames are $l_1 = 6.0$ m , $l_2 = 6.0$ m and $l_1 = 6.0$ m , $l_2 = 6.0$ m . Throughout all columns and beams, a quadratic hollow steel cross section is chosen with the dimension $0.3 * 0.3\ m^2$, and a thickness of 0.01 m. The density of the material is 7850 kg m^{-3}. The slabs are realized by various additional point masses, which are attached to the beams. They are visualized by the red marks in Fig. 1. Point masses of 8000 kg and 2000 kg are chosen for the left and the right frame system, respectively. This leads to two frame systems with significantly different dynamic behavior. Rayleigh-damping regarding the 2nd and 5th global mode with a damping ratio of $\zeta = 4\ \%$ is assumed. It must be noted that, in this paper, we focused on creating an illustrative numerical example for the demonstration of the new substructure formulation adapted to earthquake-induced collision of structures. Thus, the choice of the geometrical measures of cross sections is not optimized according to a structural design analysis. The example in Fig. 1 serves as an academic benchmark example to compare state-of-the art methods with the proposed substructure formulation.

As clearly seen in Fig. 1, the heights of the two frame systems are not equal. The application of a multi-story-shear-frame system with concentrated mass in the slabs has already been done regarding this general situation (Jankowski 2009). The whole structure is discretized by two-node beam elements. In particular, the frame systems are discretized by two-node structural beam elements with lumped mass and three degrees of freedom per node, i.e., axial and tangential local displacements and rotation. Hermitian polynomials of third order are chosen for the

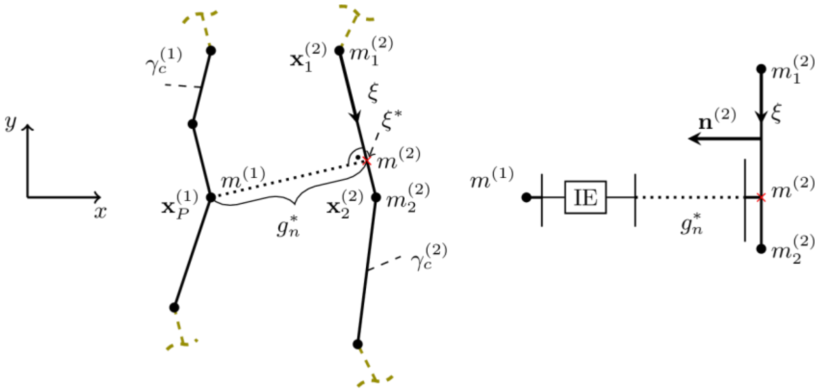

Fig. 2 Illustration of the gap function based on CPP, the lumped masses, the interpolation of the corresponding pounding mass at the master side and the embedding of the nonlinear viscoelastic impact element (IE)

shape functions for the degrees of freedom in transversal and rotational directions (Bathe 2006), i.e., for η and φ, respectively. Linear shape functions are chosen for the degrees of freedom in longitudinal direction, i.e., ξ. This is shown in the left upper corner of Fig. 1. This leads to a system with 796 degrees of freedom in total. For the realization of the finite element implementation, we use our in-house tool, which has been verified using the commercial software package ABAQUS® (Shi *et al*. 2018). In order to check the accuracy of the finite element model, a reference solution using the state-of-the art central difference time integration scheme, is performed. No noticeable difference in the response functions (not shown in this paper) is observed.

3. A node-to-surface pounding formulation using linear and nonlinear impact elements

The regions, where potential collisions can take place during ground excitation, are defined by master and slave surfaces on the master and slave bodies, respectively. Conventionally, the slave body is labeled by superscript index $^{(1)}$ and the master body by superscript index $^{(2)}$. In this context, we define the potential contact surfaces between the master frame S_1 and the slave frame S_2 as $\Gamma_c^{(1)}$ and $\Gamma_c^{(2)}$in the un-deformed configuration, respectively (cf. Fig. 1). In Fig. 2, the slave surface in the current configuration is defined as $\gamma_c^{(1)}$ and the master surface in the current configuration is defined as $\gamma_c^{(2)}$. Based on the node-to-surface formulation, the gap function g_n^* is defined as the minimum distance between the slave point $\mathbf{x}_P^{(1)}$ and the opposite point on the corresponding master element of the discretized system in the current configuration, see Fig. 2, which is also called closest point projection (CPP) (Wriggers 2006). The magnitude $m^{(1)}$ is the lumped mass at the slave node $\mathbf{x}_P^{(1)}$. The corresponding pounding mass at the master side is derived from the linear interpolation of the opposite lumped masses $m_1^{(2)}$ and $m_2^{(2)}$ of the corresponding master element. The impact element (IE), which bridges the non-conforming meshes, cf. Choi and Lee (2003), is defined between these two masses ($m^{(1)}$ and $m^{(2)}$) to describe the constitutive pounding law.

Adapting the definition of the gap function to practical structural pounding problems, the possible candidate element for collision on the master surface defined by the nodes $\mathbf{x}_1^{(2)}$ and $\mathbf{x}_2^{(2)}$, characterized by the parameter ξ, can be written in parametric representation as

$$\mathbf{x}^{(2)}(\xi) = \mathbf{x}_1^{(2)} + \left(\mathbf{x}_2^{(2)} - \mathbf{x}_1^{(2)}\right)\xi\,. \tag{1}$$

The line between the possible collision point on the master element and the corresponding collision point on the slave surface $\mathbf{x}_P^{(1)}$ is defined introducing the gap parameter g_n as

$$\mathbf{x}^{(2)}(g_n) = \mathbf{x}_P^{(1)} + g_n\,\mathbf{n}^{(2)}\,. \tag{2}$$

In this equation, $\mathbf{n}^{(2)}$ denotes the unit normal vector with respect to the master element surface, which is directed per definition towards the corresponding node on the slave surface $\mathbf{x}_P^{(1)}$ in the initial configuration, where the frame systems are separated, and no contact is prescribed. The two unknowns of the system of Eqs. (1) and (2) are the variables g_n and ξ. Solving these two equations leads to the solutions g_n^* and ξ^*, if an intersection point is found. Furthermore, if the condition $0 \le \xi^* \le 1$ is fulfilled, a pair of a slave node and a corresponding master element is found. Through the definition of $\mathbf{n}^{(2)}$, the gap parameter g_n^* is negative if no collision is detected. Contrariwise, it is positive if a collision is detected, i.e., if penetration occurs. This procedure must be repeated for each slave node. The brute-force-search method, in which every possible contact pair is checked, is used to find the correct nearest master element, as the total loop over the number of slave nodes is easily manageable for the academic example.

The above-mentioned definition of the gap function enables the introduction of the Macaulay bracket (Wriggers 2006) for the description of the collisions

$$\langle g_n^* \rangle := \begin{cases} g_n^* & \text{if } g_n^* \ge 0 \\ 0 & \text{if } g_n^* < 0 \end{cases}. \tag{3}$$

This definition can be applied for the description of an arbitrary constitutive collision law, represented by an impact element (IE), shown in the right subplot of Fig. 2.

Four impact elements are presented together with the

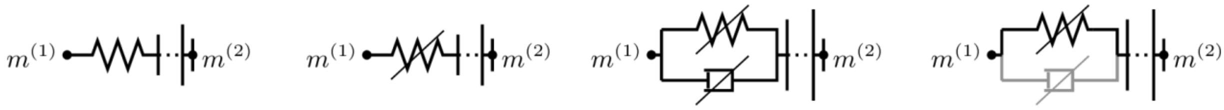

Fig. 3 Four different impact elements (from left to right: linear elastic, Hertz-nonlinear, Hertzdamp and nonlinear viscoelastic element)

node-to-surface pounding formulations. This includes the energy-conserving linear spring and the nonlinear Hertz elements as well as the energy-dissipating Hertz-Damp and the nonlinear viscoelastic model.

The linear pounding element represents the simplest collision formulation (cf. first subplot of Fig. 3). If the gap parameter becomes positive, i.e., penetration is detected, a linear spring is active, defined by the spring stiffness parameter ϵ. The collision force is then described by using definition in Eq. (3)

$$F^c = \epsilon \langle g_n^* \rangle \ . \tag{4}$$

In this paper, a value of $1.5 \cdot 10^9\ [N/m]$ is chosen for the parameter ϵ. A significant improvement is achieved using Hertz's law (Ye *et al*. 2009). The collision force increases nonlinearly with increasing penetration

$$F^c = k_h \langle g_n^* \rangle^{\frac{3}{2}} \ . \tag{5}$$

The parameter k_h is the nonlinear spring stiffness, which describes the hardness of the impact surface. Regarding the illustrative example, a value of $2.0 \cdot 10^9\ [N/m^{1.5}]$ is chosen (Jankowski 2005, Ye *et al*. 2009). The corresponding rheological element is depicted in the second subplot of Fig. 3. The nonlinear Hertz spring within the rheological model is indicated by crossing out the conventional spring sign.

The disadvantage of the above-mentioned two pounding elements is the lack of describing energy dissipation.

Introducing the Hertzdamp formulation (Muthukumar and DesRoches 2006), a nonlinear dashpot element is added in parallel to the nonlinear Hertz spring. A possible rheological model is shown in the third subplot of Fig. 3. The collision force is described by

$$F^c = k_h \langle g_n^* \rangle^{\frac{3}{2}} + c_h\, \dot{g}_n^*. \tag{6}$$

The variable $\dot{g}_n$ denotes the gap velocity and the magnitude c_h defines the nonlinear damping coefficient, which is calculated by

$$c_h = \zeta_{hd} \langle g_n^* \rangle^{\frac{3}{2}}. \tag{7}$$

The damping constant ζ_{hd} is expressed by the nonlinear spring stiffness k_h, the coefficient of restitution e and the relative velocity of the two collision points

$$\zeta_{hd} = \frac{3\, k_h\, (1-e^2)}{4\, (\dot{x}^{(1)} - \dot{x}^{(2)})}. \tag{8}$$

The coefficient of restitution e is chosen to be 0.7. This agrees well with the studies of Anagnostopoulos (Anagnostopoulos and Spiliopoulos 1992), who proposes values between 0.5 and 0.75.

Regarding Jankowski's formulation (Jankowski 2005), energy dissipation takes place mainly during the approach time period, i.e., $\dot{g} > 0$. A nonlinear dashpot element is added in parallel with the nonlinear Hertz spring, which is only active during the approach time period. In the rightmost subplot of Fig. 3, a possible rheological model of the nonlinear viscoelastic element is depicted. In this figure, the nonlinear dashpot is color-coded in gray, as it is only active during the approach time period. The collision force is defined as

$$F^c = \overline{\beta}\, \langle g_n^* \rangle^{\frac{3}{2}} + \overline{c}(t)\, \langle \dot{g}_n^* \rangle \ . \tag{9}$$

Herein, the magnitude $\overline{\beta}$ is the impact stiffness parameter. For steel to steel pounding, impact stiffness $\overline{\beta} = 1.03 \cdot 10^{10} [N/m^{1.5}]$ is chosen according to the experimental study of Jankowski (Jankowski 2005). The magnitude $\overline{c}(t)$ is the impact damping coefficient, which is obtained within every integration time step by the formula

$$\overline{c}(t) = 2\overline{\xi} \sqrt{\overline{\beta}\, \sqrt{\langle g_n^* \rangle}\, \frac{m^{(1)} m^{(2)}}{m^{(1)} + m^{(2)}}} \ . \tag{10}$$

The pounding force is also dependent on the two discrete masses $m^{(1)}$ and $m^{(2)}$. Regarding the node-to-surface formulation adapted to structural pounding, the mass $m^{(1)}$ refers to the nodal lumped mass of the corresponding slave node. The lumped mass $m^{(2)}$ is evaluated by interpolation functions of the nodal masses of the corresponding master element

$$m^{(2)}(\xi^*) = (1 - \xi^*)\, m_1^{(2)} + \xi^*\, m_2^{(2)}. \tag{11}$$

As presented in this equation, a linear interpolation function is assumed. Applying this new formulation, the time dependent discrete mass $m^{(2)}$ is introduced. This fictive mass is depicted in the left and the right subplot of Fig. 2. The magnitude $\overline{\xi}$ denotes a damping ratio related to the given coefficient of restitution, e. The relation between $\overline{\xi}$ and e for the nonlinear viscoelastic model is given by the equation (Jankowski 2006)

$$\overline{\xi} = \frac{9\sqrt{5}}{2}\, \frac{1-e^2}{e(e(9\pi - 16) + 16)}. \tag{12}$$

This impact element shows good agreements with experiments about steel to steel pounding (Jankowski 2006).

Having defined the node-to-surface impact formulations, a non-conform discretization of two frame systems is possible.

4. Efficient treatment of the pounding problem using a hierarchical substructure formulation

4.1 The full system-numerical barrier

Inserting the constitutive pounding laws, proposed in the previous subsection, into the finite element formulation, leads to the set of equations of motion for the discretized dynamic system

$$\mathbf{M}\ddot{\mathbf{u}} + \mathbf{C}\dot{\mathbf{u}} + \mathbf{K}\mathbf{u} + \mathbf{F}^{\mathbf{c}}(\mathbf{u}, \dot{\mathbf{u}}) = -\mathbf{M}\mathbf{f}\ddot{x}_g. \tag{13}$$

In this equation, $\mathbf{M}$, $\mathbf{C}$ and $\mathbf{K}$ are the global mass, damping and stiffness matrices, respectively (Wriggers 2006, Bathe 2006, Anagnostopoulos and Spiliopoulos 1992, Laursen 2003). If energy-conserving pounding models are applied, the contact force $\mathbf{F}^{\mathbf{c}}$ is directly expressed as a function of the displacement field. In case of the Hertzdamp or the nonlinear viscoelastic impact element, the contact force is also dependent on the velocity field. The contact force is active during the collisions. Within these time periods, it couples the two frame systems following the phenomenological collision rules. The right-hand side of Eq. (13) refers to the excitation term due to ground acceleration $\ddot{x}_g$ (Chopra 2007), introducing the influence vector $\mathbf{f}$. Regarding the upcoming parts of the paper, this inertia term is abbreviated by the equivalent force $\mathbf{F}(t)$. In case of earthquake induced ground acceleration, the initial conditions are assumed to be zero for both the displacements and velocities.

The solution of Eq. (13) is derived using the explicit second-order central difference integration scheme. The approximations of velocity and acceleration are defined by the second-order forward and backward Taylor expansion

$$\dot{\mathbf{u}}_k = \frac{\mathbf{u}_{k+1} - \mathbf{u}_{k-1}}{2\Delta t}, \quad \ddot{\mathbf{u}}_k = \frac{\mathbf{u}_{k-1} - 2\,\mathbf{u}_k + \mathbf{u}_{k+1}}{\Delta t^2}. \tag{14}$$

Inserting the approximations in Eq. (14) into the equation of motion Eq. (13), leads to the explicit iteration representation of the displacement field at time instant t_{k+1}

$$\begin{aligned} &\left(\frac{1}{\Delta t^2}\mathbf{M} + \frac{1}{2\Delta t}\mathbf{C}\right)\mathbf{u}_{k+1} \\ &= \mathbf{F}_k - \left(\mathbf{K} - \frac{2}{\Delta t^2}\mathbf{M}\right)\mathbf{u}_k \\ &- \left(\frac{1}{\Delta t^2}\mathbf{M} + \frac{1}{2\Delta t}\mathbf{C}\right)\mathbf{u}_{k-1} + \mathbf{F}_k^c. \end{aligned} \tag{15}$$

The central difference integration scheme is conditionally stable. If the chosen integration time step is larger than a critical value, the algorithm becomes unstable and the solution grows exponentially to infinity. The critical time step depends on the highest natural frequency $\omega_{\max}$ of the pounding system

$$\Delta t \leq t_{\text{crit}} = \frac{2}{\omega_{\max}}. \tag{16}$$

In case of high-dimensional systems, considerably small-time steps are required, as the highest eigenfrequency of the fine system is large. This effect reduces the computation speed significantly. A physically-motivated reduction of the degrees of freedom can enlarge the critical time step. Thus, a new model order reduction strategy, using the Craig-Bampton technique, adapted to complex pounding formulations, is introduced in the upcoming subsection.

4.2 The reduced system-an efficient hierarchical substructure formulation

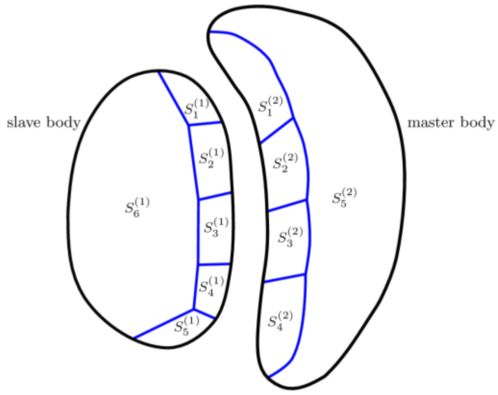

Fig. 4 Substructures of the pounding system

In this subsection, a substructure method, applied to structural pounding problems, using the Craig-Bampton method, is introduced. In order to present the general idea of the new strategy, two bodies are introduced, which collide potentially (cf. Fig. 4). The general objective of model order reduction is to significantly lower the computational effort by preserving a sufficiently accurate representation of the dynamic system. Regarding the new strategy, the focus is to provide an accurate representation of the dynamic system within areas of great interest and less accurate descriptions relatively far away from these areas. Concerning pounding problems, the areas of great interest are the potential collision surfaces, as they have a significant influence on the overall dynamic behavior of the system.

We arbitrarily define the left body as the slave and the right body as the master. Both the slave and the master bodies are independently divided into substructures, as shown in Fig. 4, so that the collision area is described as detailed as possible.

The substructure technique combined with the Craig-Bampton method is exemplarily introduced for the slave side, as the method is analogously applied to the master side. For the whole slave body, the set of equations of motion can be written as

$$\begin{aligned} \mathbf{M}^{(1)}\ddot{\mathbf{u}}^{(1)} + \mathbf{C}^{(1)}\dot{\mathbf{u}}^{(1)} + \mathbf{K}^{(1)}\mathbf{u}^{(1)} + \mathbf{F}^{\mathbf{c}(1)}(\mathbf{u}, \dot{\mathbf{u}}) \\ = \mathbf{F}^{(1)}(t). \end{aligned} \tag{17}$$

Considering the i^{th} substructure $S_i^{(1)}$ (i=1,2,...,r, regarding the demonstrated example r=6), the set of equations of motion is written as

$$\begin{aligned} \mathbf{M}_i^{(1)}\ddot{\mathbf{u}}_i^{(1)} + \mathbf{C}_i^{(1)}\dot{\mathbf{u}}_i^{(1)} + \mathbf{K}_i^{(1)}\mathbf{u}_i^{(1)} + \mathbf{F}_i^{c(1)}(\mathbf{u}, \dot{\mathbf{u}}) \\ = \mathbf{F}_i^{(1)}(t) + \mathbf{G}_i^{(1)}(t), \end{aligned} \tag{18}$$

where the additional term $\mathbf{G}_i^{(1)}(t)$ refers to the connection force of the i^{th} substructure with one or more neighbor substructures. For each substructure $S_i^{(1)}$, the degrees of freedom $\mathbf{u}_i^{(1)}$ are decomposed into two groups, the interface degrees of freedom $\mathbf{u}_{i,R}^{(1)}$ and the internal degrees of freedom $\mathbf{u}_{i,I}^{(1)}$:

$$\mathbf{u}_i^{(1)} = \begin{bmatrix} \mathbf{u}_{i,R}^{(1)} \\ \mathbf{u}_{i,I}^{(1)} \end{bmatrix}. \tag{19}$$

Inserting this decomposition (19) into Eq. (18), the set of equations of motion for the i^{th} substructure is reformulated as

$$\begin{bmatrix} \mathbf{M}^{(1)}_{i,RR} & \mathbf{M}^{(1)}_{i,RI} \\ \mathbf{M}^{(1)}_{i,IR} & \mathbf{M}^{(1)}_{i,II} \end{bmatrix} \begin{bmatrix} \ddot{\mathbf{u}}^{(1)}_{i,R} \\ \ddot{\mathbf{u}}^{(1)}_{i,I} \end{bmatrix} + \begin{bmatrix} \mathbf{C}^{(1)}_{i,RR} & \mathbf{C}^{(1)}_{i,RI} \\ \mathbf{C}^{(1)}_{i,IR} & \mathbf{C}^{(1)}_{i,II} \end{bmatrix} \begin{bmatrix} \dot{\mathbf{u}}^{(1)}_{i,R} \\ \dot{\mathbf{u}}^{(1)}_{i,I} \end{bmatrix} + \begin{bmatrix} \mathbf{K}^{(1)}_{i,RR} & \mathbf{K}^{(1)}_{i,RI} \\ \mathbf{K}^{(1)}_{i,IR} & \mathbf{K}^{(1)}_{i,II} \end{bmatrix} \begin{bmatrix} \mathbf{u}^{(1)}_{i,R} \\ \mathbf{u}^{(1)}_{i,I} \end{bmatrix} + \begin{bmatrix} \mathbf{F}^{c\,(1)}_{i,R} \\ \mathbf{F}^{c\,(1)}_{i,I} \end{bmatrix} = \begin{bmatrix} \mathbf{F}^{(1)}_{i,R}(t) \\ \mathbf{F}^{(1)}_{i,I}(t) \end{bmatrix} + \begin{bmatrix} \mathbf{G}^{(1)}_{i,R}(t) \\ \mathbf{G}^{(1)}_{i,I}(t) = \mathbf{0} \end{bmatrix} . \tag{20}$$

Since the internal degrees of freedom are isolated from other substructures, the connection forces $\mathbf{G}^{(1)}_{i,I}(t)$ between the internal degrees of freedom and other substructures are zero. Collecting the set of all equations of motion for all substructures and reordering the degrees of freedom delivers the modified expanded set of equations of motion for the whole slave body

$$\underbrace{\begin{bmatrix} \mathbf{M}^{(1)}_{1,RR} & & \mathbf{M}^{(1)}_{1,RI} & \\ & \ddots & & \ddots \\ & \mathbf{M}^{(1)}_{r,RR} & & \mathbf{M}^{(1)}_{r,RI} \\ \mathbf{M}^{(1)}_{1,IR} & & \mathbf{M}^{(1)}_{1,II} & \\ & \ddots & & \ddots \\ & \mathbf{M}^{(1)}_{r,IR} & & \mathbf{M}^{(1)}_{r,II} \end{bmatrix}}_{\widetilde{\mathbf{M}}^{(1)}} \underbrace{\begin{bmatrix} \ddot{\mathbf{u}}^{(1)}_{1,R} \\ \vdots \\ \ddot{\mathbf{u}}^{(1)}_{r,R} \\ \ddot{\mathbf{u}}^{(1)}_{1,I} \\ \vdots \\ \ddot{\mathbf{u}}^{(1)}_{r,I} \end{bmatrix}}_{\ddot{\widetilde{\mathbf{u}}}^{(1)}} + \tilde{\mathbf{C}}^{(1)} \underbrace{\begin{bmatrix} \dot{\mathbf{u}}^{(1)}_{1,R} \\ \vdots \\ \dot{\mathbf{u}}^{(1)}_{r,R} \\ \dot{\mathbf{u}}^{(1)}_{1,I} \\ \vdots \\ \dot{\mathbf{u}}^{(1)}_{r,I} \end{bmatrix}}_{\dot{\widetilde{\mathbf{u}}}^{(1)}} + \widetilde{\mathbf{K}}^{(1)} \underbrace{\begin{bmatrix} \mathbf{u}^{(1)}_{1,R} \\ \vdots \\ \mathbf{u}^{(1)}_{r,R} \\ \mathbf{u}^{(1)}_{1,I} \\ \vdots \\ \mathbf{u}^{(1)}_{r,I} \end{bmatrix}}_{\widetilde{\mathbf{u}}^{(1)}} + \tilde{\mathbf{F}}^{c\,(1)}(\widetilde{\mathbf{u}}, \dot{\widetilde{\mathbf{u}}}) = \tilde{\mathbf{F}}^{(1)}(t) + \underbrace{\begin{bmatrix} \mathbf{G}^{(1)}_{1,R} \\ \vdots \\ \mathbf{G}^{(1)}_{r,R} \\ \mathbf{0} \\ \vdots \\ \mathbf{0} \end{bmatrix}}_{\widetilde{\mathbf{G}}^{(1)}(t)} . \tag{21}$$

The expanded and reordered damping $\tilde{\mathbf{C}}^{(1)}$ and stiffness matrices $\widetilde{\mathbf{K}}^{(1)}$ have the same structure as the expanded and reordered mass matrix $\widetilde{\mathbf{M}}^{(1)}$. The reordered expanded set of equations of motion for the slave side is then written as

$$\widetilde{\mathbf{M}}^{(1)}\ddot{\widetilde{\mathbf{u}}}^{(1)} + \tilde{\mathbf{C}}^{(1)}\dot{\widetilde{\mathbf{u}}}^{(1)} + \widetilde{\mathbf{K}}^{(1)}\widetilde{\mathbf{u}}^{(1)} + \tilde{\mathbf{F}}^{c\,(1)}(\widetilde{\mathbf{u}}, \dot{\widetilde{\mathbf{u}}}) = \tilde{\mathbf{F}}^{(1)}(t) + \widetilde{\mathbf{G}}^{(1)}(t). \tag{22}$$

The expansion of the slave body into substructures results in extra degrees of freedom, as the degrees of freedom at the connecting nodes are counted repeatedly. In order to assemble the substructures, a Boolean transformation matrix is introduced. The Boolean transformation between the expanded degrees of freedom $\widetilde{\mathbf{u}}^{(1)}$ and the reordered global degrees of freedom $\hat{\mathbf{u}}^{(1)}$ is easily derived since the compatibility condition at the interface must be fulfilled

$$\underbrace{\begin{bmatrix} \mathbf{u}^{(1)}_{1,R} \\ \vdots \\ \mathbf{u}^{(1)}_{r,R} \\ \mathbf{u}^{(1)}_{1,I} \\ \vdots \\ \mathbf{u}^{(1)}_{r,I} \end{bmatrix}}_{\widetilde{\mathbf{u}}^{(1)}} = \underbrace{\begin{bmatrix} \mathbf{B}^{(1)}_{1} & & & \\ \vdots & & & \\ \mathbf{B}^{(1)}_{r} & & & \\ & \mathbf{I} & & \\ & & \ddots & \\ & & & \mathbf{I} \end{bmatrix}}_{\mathbf{B}^{(1)}} \underbrace{\begin{bmatrix} \mathbf{u}^{(1)}_{R} \\ \mathbf{u}^{(1)}_{1,\mathrm{I}} \\ \vdots \\ \mathbf{u}^{(1)}_{r,\mathrm{I}} \end{bmatrix}}_{\hat{\mathbf{u}}^{(1)}} . \tag{23}$$

In other words, the Boolean matrix $\mathbf{B}^{(1)}_{i}$ of the i^{th} substructure transfers the interface degrees of freedom of the whole slave body $\mathbf{u}^{(1)}_{R}$ to the substructure interface degrees of freedom $\mathbf{u}^{(1)}_{i,R}$. The interface forces of all substructures vanish by inserting Eq. (23) into the expanded equations of motion Eq. (22) and left multiplication of the transpose of $\mathbf{B}^{(1)}$. This operation leads to

$$\underbrace{\mathbf{B}^{(1)^{\mathrm{T}}}\widetilde{\mathbf{M}}^{(1)}\mathbf{B}^{(1)}}_{\widehat{\mathbf{M}}^{(1)}}\ddot{\hat{\mathbf{u}}}^{(1)} + \underbrace{\mathbf{B}^{(1)^{\mathrm{T}}}\tilde{\mathbf{C}}^{(1)}\mathbf{B}^{(1)}}_{\hat{\mathbf{C}}^{(1)}}\dot{\hat{\mathbf{u}}}^{(1)} + \underbrace{\mathbf{B}^{(1)^{\mathrm{T}}}\widetilde{\mathbf{K}}^{(1)}\mathbf{B}^{(1)}}_{\widehat{\mathbf{K}}^{(1)}}\hat{\mathbf{u}}^{(1)} + \underbrace{\mathbf{B}^{(1)^{\mathrm{T}}}\tilde{\mathbf{F}}^{c\,(1)}(\hat{\mathbf{u}}, \dot{\hat{\mathbf{u}}})}_{\hat{\mathbf{F}}^{c\,(1)}(\hat{\mathbf{u}}, \dot{\hat{\mathbf{u}}})} = \underbrace{\mathbf{B}^{(1)^{\mathrm{T}}}\tilde{\mathbf{F}}^{(1)}(t)}_{\hat{\mathbf{F}}^{(1)}(t)} + \underbrace{\mathbf{B}^{(1)^{\mathrm{T}}}\widetilde{\mathbf{G}}^{(1)}}_{\mathbf{0}} . \tag{24}$$

Eq. (24) is then rewritten as

$$\widehat{\mathbf{M}}^{(1)}\ddot{\hat{\mathbf{u}}}^{(1)} + \hat{\mathbf{C}}^{(1)}\dot{\hat{\mathbf{u}}}^{(1)} + \widehat{\mathbf{K}}^{(1)}\hat{\mathbf{u}}^{(1)} + \hat{\mathbf{F}}^{c\,(1)}(\hat{\mathbf{u}}, \dot{\hat{\mathbf{u}}}) = \hat{\mathbf{F}}^{(1)}(t) . \tag{25}$$

The above decomposition of the degrees of freedom in Eq. (19) gives the possibility to truncate the target-oriented degrees of freedom. The main idea of the method in this paper is to truncate the internal degrees of freedom, which are separated from the interface degrees of freedom

$$\left[\mathbf{K}^{(1)}_{i,II} - \omega^{(1)^2}_{i,II,m}\mathbf{M}^{(1)}_{i,II}\right]\boldsymbol{\varphi}^{(1)}_{i,II,m} = \mathbf{0} . \tag{26}$$

Only a small number of the lower internal modes are considered, whereas the higher modes are truncated. The reduced modal degrees of freedom are defined as $\mathbf{z}^{(1)}_{i}$. The Craig-Bampton transformation into the reduced space regarding one substructure is written as

$$\mathbf{u}^{(1)}_{i} = \begin{bmatrix} \mathbf{u}^{(1)}_{i,R} \\ \mathbf{u}^{(1)}_{i,I} \end{bmatrix} = \begin{bmatrix} \mathbf{I} & \mathbf{0} \\ \boldsymbol{\Phi}^{(1)}_{i,CB} & \boldsymbol{\Phi}^{(1)}_{i} \end{bmatrix} \begin{bmatrix} \mathbf{u}^{(1)}_{i,R} \\ \mathbf{z}^{(1)}_{i} \end{bmatrix} . \tag{27}$$

The objective is that the dimension of $\mathbf{z}^{(1)}_{i}$ should be significantly smaller than the dimension of the unreduced internal degrees of freedom $\mathbf{u}^{(1)}_{i,I}$. This truncation process is carried out for the internal degrees of freedom of all substructures

$$\underbrace{\begin{bmatrix} \mathbf{u}^{(1)}_{R} \\ \mathbf{u}^{(1)}_{1,I} \\ \mathbf{u}^{(1)}_{2,I} \\ \vdots \\ \mathbf{u}^{(1)}_{r,I} \end{bmatrix}}_{\hat{\mathbf{u}}^{(1)}} = \underbrace{\begin{bmatrix} \mathbf{I} & & & & \\ \boldsymbol{\Phi}^{(1)}_{1,CB} & \boldsymbol{\Phi}^{(1)}_{1} & & & \\ \boldsymbol{\Phi}^{(1)}_{2,CB} & & \boldsymbol{\Phi}^{(1)}_{2} & & \\ \vdots & & & \ddots & \\ \boldsymbol{\Phi}^{(1)}_{r,CB} & & & & \boldsymbol{\Phi}^{(1)}_{r} \end{bmatrix}}_{\boldsymbol{\beta}^{(1)}} \underbrace{\begin{bmatrix} \mathbf{u}^{(1)}_{R} \\ \mathbf{z}^{(1)}_{1} \\ \mathbf{z}^{(1)}_{2} \\ \vdots \\ \mathbf{z}^{(1)}_{r} \end{bmatrix}}_{\hat{\mathbf{z}}^{(1)}} . \tag{28}$$

This equation shows the clear relation between the reordered global degrees of freedom $\hat{\mathbf{u}}^{(1)}$, which is given in Eq. (25), and the reduced degrees of freedom $\hat{\mathbf{z}}^{(1)}$ of the slave body. The global Craig-Bampton transformation matrix for the slave side is defined as $\boldsymbol{\beta}^{(1)}$.

As mentioned above, the same reduction technique is also carried out for the master side (in total s substructures regarding the demonstrated examples $s = 5$). The expanded equations of motion for the master side can be written as

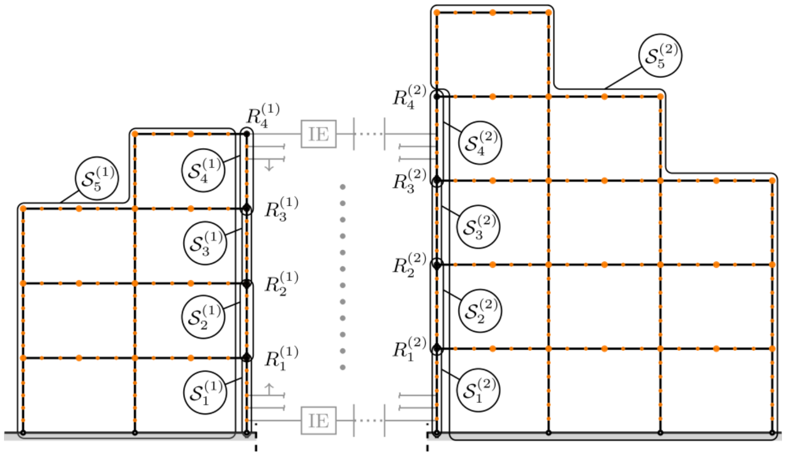

Fig. 5 Division of the substructures; definition of the interface nodes (R-nodes) in black and the internal nodes (I-nodes) in orange; coupling of impact elements (IE) in gray

$$\widehat{\mathbf{M}}^{(2)}\ddot{\widehat{\mathbf{u}}}^{(2)} + \widehat{\mathbf{C}}^{(2)}\dot{\widehat{\mathbf{u}}}^{(2)} + \widehat{\mathbf{K}}^{(2)}\widehat{\mathbf{u}}^{(2)} + \widehat{\mathbf{F}}^{c^{(2)}}\left(\widehat{\mathbf{u}}, \dot{\widehat{\mathbf{u}}}\right) = \widehat{\mathbf{F}}^{(2)}(t) \ . \tag{29}$$

An analogous relation between the reordered global degrees of freedom $\widehat{\mathbf{u}}^{(2)}$ and the reduced degrees of freedom $\hat{\mathbf{z}}^{(2)}$ of the master body is established

$$\underbrace{\begin{bmatrix} \mathbf{u}_R^{(2)} \\ \mathbf{u}_{1,I}^{(2)} \\ \mathbf{u}_{2,I}^{(2)} \\ \vdots \\ \mathbf{u}_{s,I}^{(2)} \end{bmatrix}}_{\widehat{\mathbf{u}}^{(2)}} = \underbrace{\begin{bmatrix} \mathbf{I} & & & & \\ \mathbf{\Phi}_{1,CB}^{(2)} & \mathbf{\Phi}_1^{(2)} & & & \\ \mathbf{\Phi}_{2,CB}^{(2)} & & \mathbf{\Phi}_2^{(2)} & & \\ \vdots & & & \ddots & \\ \mathbf{\Phi}_{s,CB}^{(2)} & & & & \mathbf{\Phi}_s^{(2)} \end{bmatrix}}_{\boldsymbol{\beta}^{(2)}} \underbrace{\begin{bmatrix} \mathbf{u}_R^{(2)} \\ \mathbf{z}_1^{(2)} \\ \mathbf{z}_2^{(2)} \\ \vdots \\ \mathbf{z}_s^{(2)} \end{bmatrix}}_{\hat{\mathbf{z}}^{(2)}} . \tag{30}$$

The global Craig-Bampton transformation matrix for the master side is defined as $\boldsymbol{\beta}^{(2)}$. The sorted unreduced set of equations of motion for the whole system is generated by assembling Eqs. (25) and (29)

$$\widehat{\mathbf{M}}\ddot{\widehat{\mathbf{u}}} + \widehat{\mathbf{C}}\dot{\widehat{\mathbf{u}}} + \widehat{\mathbf{K}}\widehat{\mathbf{u}} + \widehat{\mathbf{F}}^{c}\left(\widehat{\mathbf{u}}, \dot{\widehat{\mathbf{u}}}\right) = \widehat{\mathbf{F}}(t) \ , \tag{31}$$

with $\widehat{\mathbf{M}} = \begin{bmatrix} \widehat{\mathbf{M}}^{(1)} & \mathbf{0} \\ \mathbf{0} & \widehat{\mathbf{M}}^{(2)} \end{bmatrix}$, $\widehat{\mathbf{C}} = \begin{bmatrix} \widehat{\mathbf{C}}^{(1)} & \mathbf{0} \\ \mathbf{0} & \widehat{\mathbf{C}}^{(2)} \end{bmatrix}$, $\widehat{\mathbf{K}} = \begin{bmatrix} \widehat{\mathbf{K}}^{(1)} & \mathbf{0} \\ \mathbf{0} & \widehat{\mathbf{K}}^{(2)} \end{bmatrix}$, $\widehat{\mathbf{F}}^{c}\left(\widehat{\mathbf{u}}, \dot{\widehat{\mathbf{u}}}\right) = \begin{bmatrix} \widehat{\mathbf{F}}^{c^{(1)}}\left(\widehat{\mathbf{u}}, \dot{\widehat{\mathbf{u}}}\right) \\ \widehat{\mathbf{F}}^{c^{(2)}}\left(\widehat{\mathbf{u}}, \dot{\widehat{\mathbf{u}}}\right) \end{bmatrix}$, $\widehat{\mathbf{F}}(t) = \begin{bmatrix} \widehat{\mathbf{F}}^{(1)}(t) \\ \widehat{\mathbf{F}}^{(2)}(t) \end{bmatrix}$ and $\widehat{\mathbf{u}} = \begin{bmatrix} \widehat{\mathbf{u}}^{(1)} \\ \widehat{\mathbf{u}}^{(2)} \end{bmatrix}$.

The global Craig-Bampton transformation matrix for the whole system is then defined as

$$\boldsymbol{\beta} = \begin{bmatrix} \widehat{\boldsymbol{\beta}}^{(1)} \\ \widehat{\boldsymbol{\beta}}^{(2)} \end{bmatrix} \ . \tag{32}$$

Finally, applying the global Craig-Bampton transformation matrix to the global sorted unreduced equations of motion and left multiplication with the transpose of $\boldsymbol{\beta}$ leads to the reduced set of equations of motion for the whole system

$$\underbrace{\boldsymbol{\beta}^{\mathrm{T}}\widehat{\mathbf{M}}\boldsymbol{\beta}}_{\widehat{\mathbf{m}}}\ddot{\hat{\mathbf{z}}} + \underbrace{\boldsymbol{\beta}^{\mathrm{T}}\widehat{\mathbf{C}}\boldsymbol{\beta}}_{\hat{\mathbf{c}}}\dot{\hat{\mathbf{z}}} + \underbrace{\boldsymbol{\beta}^{\mathrm{T}}\widehat{\mathbf{K}}\boldsymbol{\beta}}_{\hat{\mathbf{k}}}\hat{\mathbf{z}} + \underbrace{\boldsymbol{\beta}^{\mathrm{T}}\widehat{\mathbf{F}}^{c}\left(\widehat{\mathbf{u}}, \dot{\widehat{\mathbf{u}}}\right)}_{\hat{\mathbf{f}}^{c}} = \underbrace{\boldsymbol{\beta}^{\mathrm{T}}\widehat{\mathbf{F}}(t)}_{\hat{\mathbf{f}}(t)} . \tag{33}$$

The total degrees of freedom of the low-order system $\hat{\boldsymbol{z}}$ can be significantly reduced through this transformation. Thereby, the computational efficiency is improved, on the one hand, by a smaller equations system and, on the other hand, by the fact that the critical time step is considerably enlarged.

Notice that the contact force within the full space must be updated for each time integration step. This means that the reduced solution $\hat{\boldsymbol{z}}$ must be transformed back into the global coordinates $\widehat{\mathbf{u}}$ and its time derivatives for each time step. Since the static modes and the modes of vibration are time-invariant, the mass, the stiffness and the damping matrices are determined and resorted only once *apriori* to the whole-time integration process.

5. Numerical demonstration

In this section, the numerical demonstrations of the in Section 3 presented node-to-surface pounding formulations are presented. The dynamical pounding problems are solved using the new hierarchical substructure technique.

5.1 Hierarchical definition of the substructures

Both the slave (left frame) and the master (right frame) bodies are divided into frame subsystems coupled by the contact formulation. The frame subsystems are again subdivided into substructures. Hereby, it is drawn attention to ensure a higher resolution of the substructures within the contact area and a lower resolution of substructures considerably far away from the potential collision area. Fig. 5 shows the definition of the interface nodes (R-nodes), separating the substructures, and internal nodes (I-nodes) inside each substructure. As mentioned above and shown in Fig. 5, the subdivisions show a more accurate representation within the pounding area and less accuracy in the regions of lower interest. About the hierarchical formulation, contact forces couple the frames subsystems, whereas the interface nodes combine the substructures within one frame subsystem. Each interface node has three degrees of freedom; each of them produces three interface modes. The

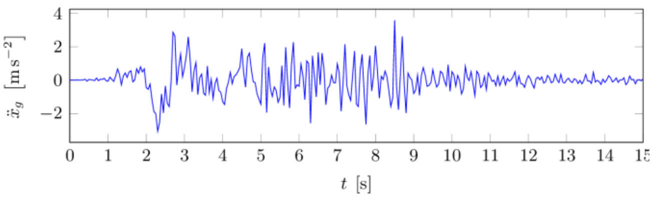

Fig. 6 Acceleration time history of the Bam earthquake excitation

first interface mode is the static response to a unit displacement in horizontal direction, whereas the degrees of freedom of all other R-nodes are fixed. The second and the third interface modes correspond to the vertical and rotational directions, respectively. Regarding substructures $S_1^{(1)}$ to $S_4^{(1)}$ on the slave side and $S_1^{(2)}$ to $S_4^{(2)}$ on the master side, four internal modes are considered. Regarding substructures $S_5^{(1)}$ and $S_5^{(2)}$, six internal modes are considered. Thus, the full system with 796 degrees of freedom is reduced to a low-order system, containing only 68 degrees of freedom.

The impact elements, introduced in Section 3, are examined for the Craig-Bampton substructure technique for the demonstrated academic model in the upcoming subsections.

5.2 System response for different impact elements under transient excitation

The Bam earthquake record (2003) is selected for the numerical demonstrations. The earthquake time record has duration of $T = 19.95s$ with $n = 400$ measurement time steps. The accelerogram is presented in Fig. 6.

The response of the adjacent frames is evaluated in terms of the displacements, the velocities, the accelerations, the gap-functions and the contact forces of the representative node, depicted in Fig. 1. Analyses are performed, applying the above-introduced four pounding models. The solutions of the classical modal truncation

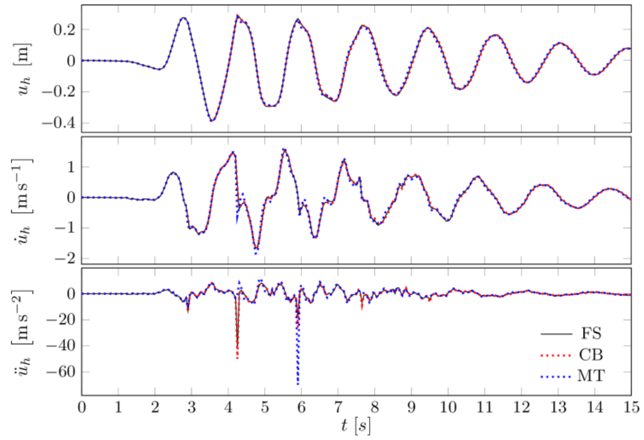

Fig. 7 Linear impact element: displacement (top), velocity (middle), acceleration (bottom) of the representative node

technique (MT) and the hierarchical substructure technique using the Craig-Bampton method (CB) are compared with the full reference solution (FS). In order to make a fair comparison, the same reduced number of degrees of freedom regarding the two reduction methods is chosen. Special attention is drawn to the comparison of the contact forces.

The displacements, velocities and accelerations are presented within the first 15 seconds of the whole excitation time history (cf. Figs. 7, 9, 11 and 13). Collisions are observed approximately between second 0 and second 10 of the whole time history concerning all impact elements, thus, the contact forces are plotted in this time period (cf. Figs. 8, 10, 12 and 14). The black lines represent the results of the full system (FS), the red dotted lines represent the results of the hierarchical Craig-Bampton method (CB) and the blue dotted lines represent the results of the modal truncation technique (MT).

For the energy-conserving linear elastic impact element, all the two reduction methods deliver good results regarding the displacements and velocities compared to the full response. However, the modal truncation technique

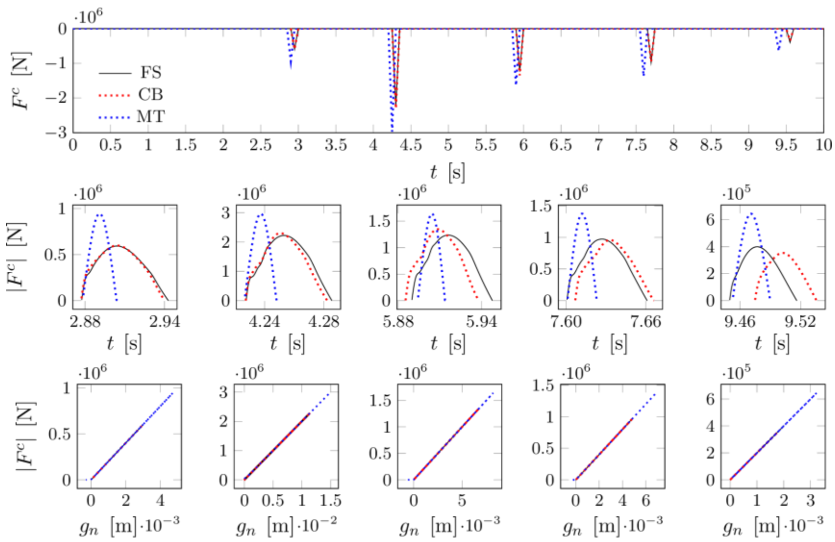

Fig. 8 Linear impact element: peak contact force (top), zoom in on the collisions (middle), gap-force relation (bottom)

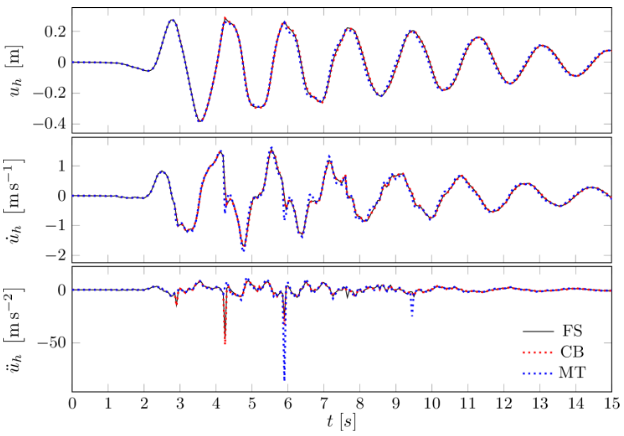

Fig. 9 Hertz-nonlinear impact element: displacement (top), velocity (middle), acceleration (bottom) of the representative node

produces a relatively large error regarding the acceleration response; see the right subplot of Fig. 7, whereas the hierarchical Craig-Bampton substructure technique approximates the accelerations well. The enlarged collision functions show that the contact force is overestimated using the modal truncation technique.

On the contrary, the hierarchical Craig-Bampton substructure technique shows a significantly better agreement with the full system force responses, as depicted in the second row of subplots of Fig. 8. Regarding the collisions two to four, the peak values of the contact forces, evaluated by the Craig-Bampton method, show a slight phase drift. It is clearly visible that the penetration of the modal truncation technique is much larger than of the full system, which leads to a significant overestimation of the contact force, as shown in the third row of Fig. 8.

The results, applying the energy-conserving Hertz-nonlinear impact element, are presented in Fig. 9.

Both the modal truncation and the hierarchical Craig-Bampton substructure technique can approximate the full solution with regard to displacements and velocities, whereas the modal truncation technique is inaccurate concerning accelerations as well as contact forces. The collision force using the classical modal truncation is overestimated by about five-fold, as shown in the last row of Fig. 10. Applying the hierarchical substructure technique, the contact force is again well approximated. The contact force of the first collision accords perfectly with the full solution. The peak values of the subsequent four collisions are still accurate, but a slight phase shift is obtained. The gap-force diagrams show the same trend as explained above.

The results of the full and reduced calculations applying the Hertzdamp model are presented in Fig. 11. The displacement and velocity response are approximated well. However, the modal truncated low-order model fails to describe the acceleration response, whereas the hierarchical Craig-Bampton technique succeeds. The peak contact force of the modal truncation technique is about twice as large as that of the full system regarding the first collisions. The corresponding gap-force diagrams are presented in the third row of Fig. 12.

The results, applying the nonlinear viscoelastic impact element, are presented in Fig. 13. Again, the modal truncation technique shows high accuracy with respect to the displacement and the velocity fields. However, it fails to describe the acceleration response. The peak values of all collisions applying the modal truncation technique are approximately twice as large as the peak values of the full system. The corresponding gap-force diagrams about all five collisions are illustrated in the last row of Fig. 14.

In summary, it can be observed that the contact force is strongly dependent on the constitutive law. However, independent on the constitutive law for the pounding force, the modal truncation technique shows the capability to estimate the displacement and velocity fields in case of the applied linear materials, as shown in Figs. 7, 9, 11 and 13. Nevertheless, it shows obvious drawbacks for the description of the acceleration response as well as the

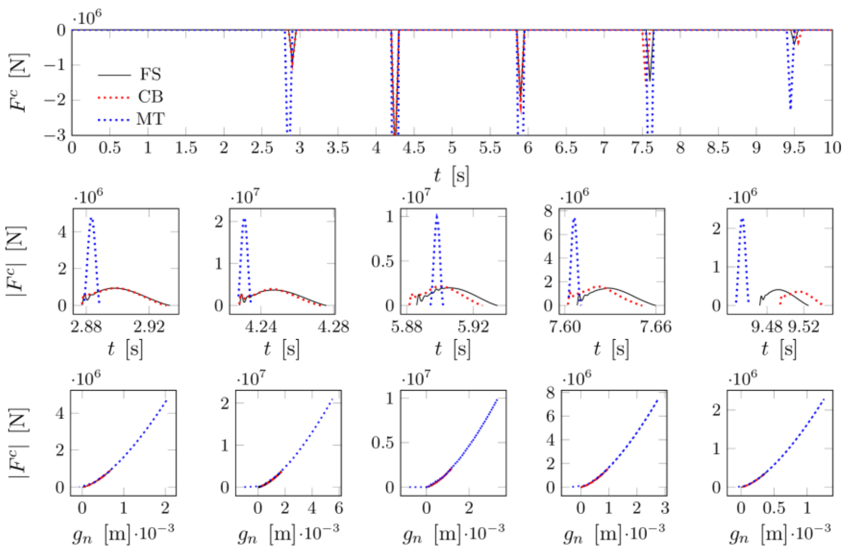

Fig. 10 Hertz-nonlinear impact element: peak contact force (top), zoom in on the collisions (middle), gap-force relation (bottom)

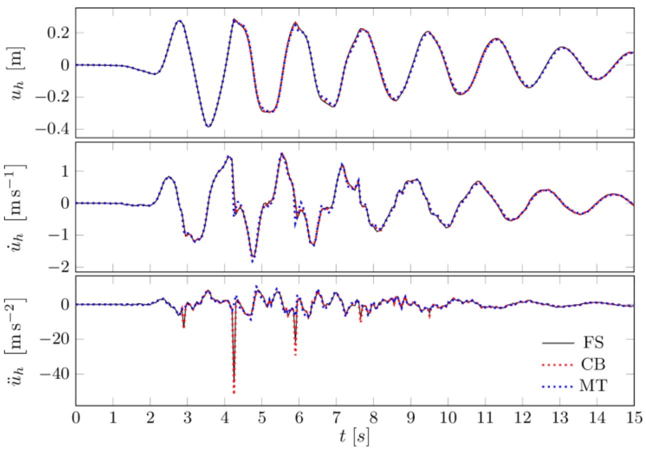

Fig. 11 Hertzdamp impact element: displacement (top), velocity (middle), acceleration (bottom) of the representative node

collision forces. The hierarchical substructure method enables an accurate description of all output quantities.

5.3 Local and global error estimation and numerical efficiency

In order to verify the accuracy and efficiency of the introduced hierarchical Craig-Bampton substructure technique for dynamic pounding problems, the results of the reduced system are qualitatively compared with the results of the full system. A separated evaluation for the linear, the Hertz-nonlinear, the Hertzdamp and the nonlinear viscoelastic impact element is carried out.

Concerning the representative node, the maximal deviation between the full and the reduced solution for all considered time steps is defined as

$$\Delta u_{\max} = \max(|u_i - \bar{u}_i|) \ . \tag{34}$$

The magnitude $\bar{u}_i$ is the full reference solution, and u_i is the solution of the reduced system at the time step i. The maximal deviations of the displacement, velocity, acceleration and contact force for the four different impact elements are summarized in Table 1. Since the maximal deviations are strongly dependent on the constitutive laws of the impact elements, a direct comparison of the results between different impact elements is not reasonable. Thus, in order to provide a meaningful comparison between the impact elements, the normalized error for the magnitudes of interest is obtained by the formula

$$\delta_{\mathbf{u}} = \frac{\|\mathbf{u}-\bar{\mathbf{u}}\|}{\bar{\mathbf{u}}} \cdot 100\% \ . \tag{35}$$

The vector $\mathbf{u}$ is the full reference solution and $\bar{\mathbf{u}}$ is the reduced solution. The normalized errors about the

Table 1 Maximum deviation of displacement $\Delta u_{\max}$, velocity $\Delta \dot{u}_{\max}$, acceleration $\Delta \ddot{u}_{\max}$, and contact force $\Delta F^{c}_{\max}$ in the horizontal direction for the four impact elements using the classic modal truncation (MT) and the Craig-Bampton substructure (CB) technique

Impact element	Method	$\Delta u_{\max}[m]$	$\Delta \dot{u}_{\max}\ [ms^{-1}]$	$\Delta \ddot{u}_{\max}[ms^{-2}]$	$\Delta F^{c}_{\max}[N]$
Linear	MT	0.026	1.100	52.463	340050
	CB	0.016	0.129	8.381	48216
Hertz-nonlinear	MT	0.038	0.936	60.151	523364
	CB	0.015	0.126	6.815	52319
Hertzdamp	MT	0.031	0.847	45.210	365930
	CB	0.016	0.143	7.493	61756
Nonlinear viscoelastic	MT	0.027	0.987	148.390	933502
	CB	0.014	0.145	6.504	57216

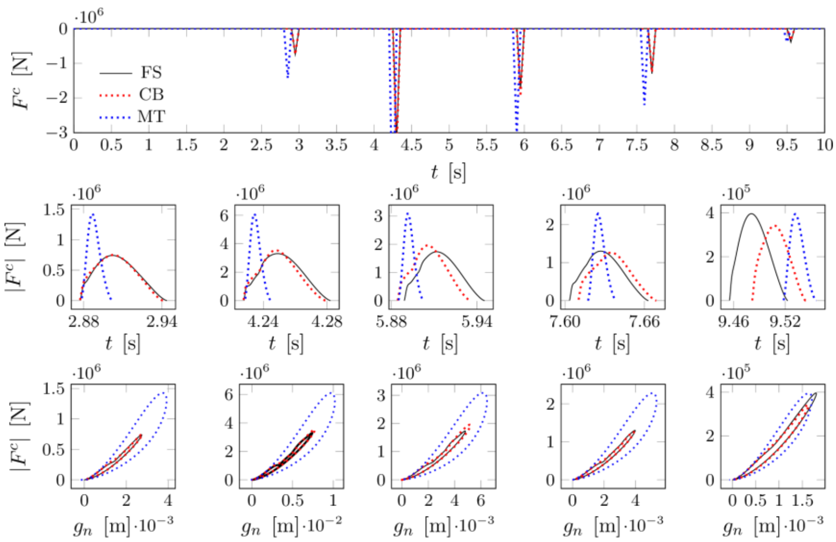

Fig. 12 Hertzdamp impact element: peak contact force (top), zoom in on the collisions (middle), gap-force relation (bottom)

Table 2 The normalized error of the displacement $\delta_{\mathbf{u}}$, velocity $\delta_{\dot{\mathbf{u}}}$, acceleration $\delta_{\ddot{\mathbf{u}}}$ and contact force $\delta_{\mathbf{F}^c}$ in the horizontal direction for the four impact elements using the classic modal truncation (MT) and the Craig-Bampton substructure (CB) technique

Impact element	Method	$\delta_{\mathbf{u}}[\%]$	$\delta_{\dot{\mathbf{u}}}[\%]$	$\delta_{\ddot{\mathbf{u}}}[\%]$	$\delta_{\mathbf{F}^c}[\%]$
Linear	MT	5.91	15.25	106.37	116.66
	CB	3.46	4.24	18.73	15.84
Hertz-nonlinear	MT	9.39	17.79	118.28	150.59
	CB	2.25	3.35	16.30	13.97
Hertzdamp	MT	6.29	14.94	74.12	96.99
	CB	3.62	4.49	16.85	17.36
Nonlinear viscoelastic	MT	5.93	15.51	220.41	233.49
	CB	3.39	4.31	12.96	14.32

Table 3 Global root-mean-square-deviation of displacement $\epsilon_{\mathbf{u}}$, velocity $\epsilon_{\dot{\mathbf{u}}}$, acceleration $\epsilon_{\ddot{\mathbf{u}}}$ and contact force $\epsilon_{\mathbf{F}^c}$ in the horizontal direction for different impact elements using the classic modal truncation (MT) and the Craig-Bampton substructure (CB) technique

Impact element	Method	$\epsilon_{\mathbf{u}}[m]$	$\epsilon_{\dot{\mathbf{u}}}\ [ms^{-1}]$	$\epsilon_{\ddot{\mathbf{u}}}[ms^{-2}]$	$\epsilon_{\mathbf{F}^c}[N]$
Linear	MT	0.949	3.818	65.597	75557
	CB	0.034	0.312	57.846	13888
Hertz-nonlinear	MT	0.940	3.781	49.540	102118
	CB	0.027	0.342	23.225	11518
Hertzdamp	MT	0.937	3.744	57.934	60958
	CB	0.035	0.312	48.609	12382
Nonlinear viscoelastic	MT	0.941	3.783	75.041	159994
	CB	0.032	0.311	22.374	12233

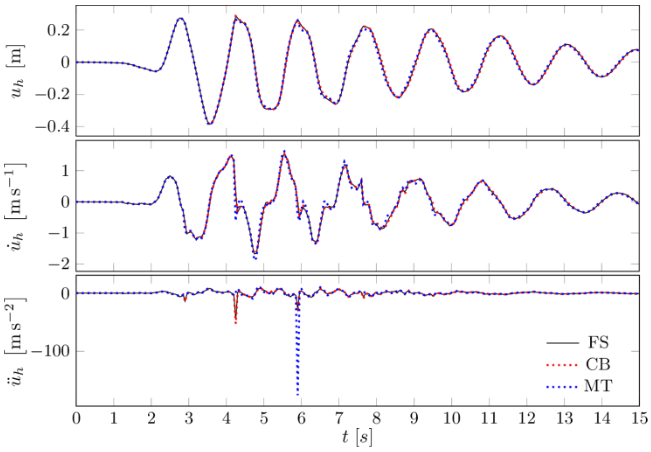

Fig. 13 Nonlinear viscoelastic impact element: displacement (top), velocity (middle), acceleration (bottom) of the representative node

representative output node are summarized in Table 2.

The relative error of the displacement using the modal truncation technique is approximately between six and ten percent and the relative error applying the hierarchical substructure technique is between two and four percent. The accuracy reduces concerning the description of the velocity response. The relative errors are around 15 and four percent regarding the modal truncation and Craig-Bampton technique, respectively. Concerning the description of the accelerations and contact forces, the classical modal truncation responses overestimate the values up to about 230 percent, whereas the Craig-Bampton technique holds the relative error still under 18 percent. It can also be seen that the modal truncation technique performs even worse for the Hertz-nonlinear and for the nonlinear viscoelastic impact elements. Interestingly, the hierarchical substructure method performs better for these two impact elements.

The error analyses above are only based on results of the representative node (cf. Fig. 1). In order to provide a global quantity, the global root-mean-square deviation (RMSD) for all nodes is evaluated. Since the time dependent vectorial magnitude of interest is arranged as a matrix $\mathbf{U}^{n\times m}$, the global error quantity $\epsilon(\mathbf{u})$ for all nodes can be calculated as

$$\epsilon(\mathbf{u}) := \sqrt{\frac{tr([\mathbf{U}-\bar{\mathbf{U}}][\mathbf{U}-\bar{\mathbf{U}}]^{\mathrm{T}})}{n\cdot m}}\ , \tag{36}$$

where m stands for the number of time steps and n for the number of global degrees of freedom.

The global error quantity is evaluated for all response quantities in Table 3. The global error for the acceleration and the contact forces shows no significant differences concerning the two reduction techniques. The reason is that the hierarchical substructure technique guarantees high accuracy within the contact areas, but it cannot guarantee high accuracy within the areas far away from the collision surfaces (cf. Fig. 5). This is also one main objective of this study.

The numerical efficiency of the two reduction methods depends firstly on the significant dimension reduction. The whole degrees of the full system with $n = 796$ are reduced to $\bar{n} = 68$. Secondly, the critical integration time step, which is calculated in Eq. (16) is significantly increased. The critical time step of the full system is

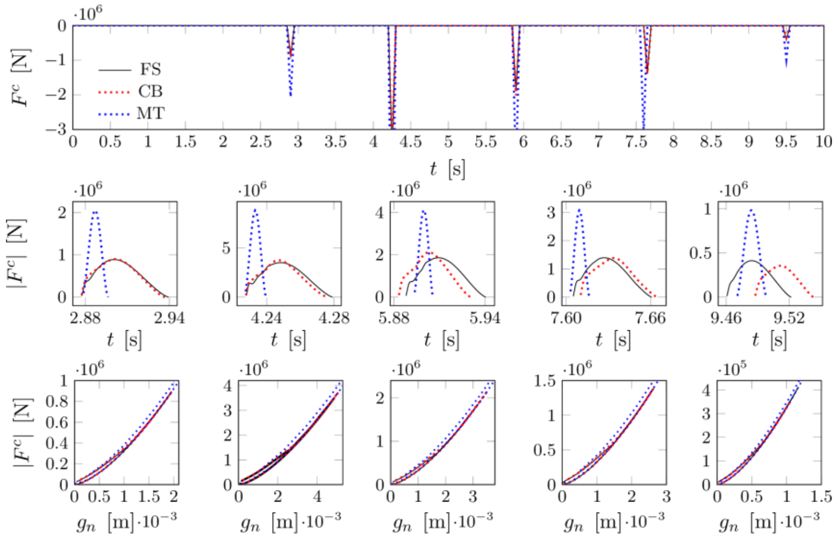

Fig. 14 Nonlinear viscoelastic impact element: peak contact force (top), zoom in on the collisions (middle), gap-force relation (bottom)

$6.7e^{-5}$ seconds, whereas the critical time step for the modal truncation method and the hierarchical Craig-Bampton method is raised to a value of $2.3e^{-5}$ and $1.2e^{-3}$ seconds, respectively.

6. Conclusions

In this paper, the efficient treatment of node-to-surface pounding formulations is discussed. Firstly, the realization of a node-to-surface pounding formulation, integrating state-of-the-art impact models, is introduced. Secondly, an efficient numerical procedure, applying a hierarchical substructure technique, is presented. Due to the clear separation of interface and internal modes, the hierarchical substructure technique reduces the physical degrees of freedom and ensures high accuracy within the contact zone. In order to verify the accuracy of the new strategy, the low-order response approximations are compared with the full reference solutions.

The results of the hierarchical substructure technique show that a significant improvement of the accelerations and the contact forces can be achieved in comparison with the results of the classical modal truncation technique. This provides only a good approximation for the displacement and velocity fields but fails regarding accelerations and contact forces. At the same time, the numerical efficiency is improved significantly. It can be concluded that the proposed substructure pounding formulation using the Craig-Bampton method offers an efficient and accurate procedure for pounding problems. A significant reduction of the degrees of freedom of the system is achieved by preserving a required level of accuracy.

Pounding of buildings is, in most cases, accompanied by damage effects caused by the high forces and stresses due to the impacts. This complex phenomenon was not considered within the introduction of the new substructure strategy in this paper. Future research should concentrate on the implementation of the substructure strategy considering collision-induced damage effects.

References

Abdel Raheem, S.E. (2014), “Mitigation measures for earthquake induced pounding effects on seismic performance of adjacent buildings”, *Bull. Earthq. Eng.*, **12**, 1705-1724. https://doi.org/10.1007/s10518-014-9592-2.

Aldaikh, H., Alexander, N.A., Ibraim, E. and Oddbjornsson, O. (2015), “Two dimensional numerical and experimental models for the study of structure-soil-structure interaction involving three buildings”, *Comput. Struct.*, **150**, 79-91. https://doi.org/10.1016/j.compstruc.2015.01.003.

Anagnostopoulos, S.A. (1992), “Equivalent viscous damping for modeling inelastic impacts in earthquake pounding problems”, *Earthq. Eng. Struct. Dyn.*, **33**,897-902. https://doi.org/10.1002/eqe.377.

Anagnostopoulos, S.A. and Spiliopoulos, K.V. (1992), “An investigation of earthquake induced pounding between adjacent buildings”, *Earthq. Eng. Struct. Dyn.*, **21**, 289-302. https://doi.org/10.1002/eqe.4290210402.

Bamer, F. (2018), “A Hertz-pounding formulation with a nonlinear damping and a dry friction element”, *Acta Mechanica*, https://10.1007/s00707-018-2233-0.

Bamer, F. and Bucher, C. (2012), “Application of the proper orthogonal decomposition for linear and nonlinear structures under transient excitation”, *Acta Mechanica*, **223**(12), 2549-2563. https://doi.org/10.1007/s00707-012-0726-9.

Bamer, F. and Markert B. (2018), “A nonlinear visco-elastoplastic model for structural pounding”, *Earthq. Eng. Struct. Dyn.*, **229**(11), 4485-4494. https://doi:10.1002/eqe.3095.

Bamer, F. and Markert, B. (2017), “An efficient response identification strategy for nonlinear structures subject to non-stationary generated seismic excitations”, *Mech. Bas. Des. Struct. Mach.*, **45**(3), 313-330. https://doi:10.1080/15397734.2017.131726.

Bamer, F., Kazhemi, A.A. and Bucher, C. (2017), “A new model order reduction strategy adapted to nonlinear problems in earthquake engineering”, *Earthq. Eng. Struct. Dyn.*, **46**(4), 537-559. https://doi.org/10.1002/eqe.2802.

Bamer, F., Shi, J. and Markert, B. (2017), “Efficient solution of the multiple seismic pounding problem using hierarchical substructure techniques", *Comput. Mech.*, **62**(4), 761-782. https://doi: 10.1007/s00466-017-1525-x.

Barbato, M. and Tubaldi, E. (2013), "A probabilistic performance-based approach for mitigating the seismic pounding risk between adjacent buildings", *Earthq. Eng. Struct. Dyn.*, **42**, 1203-1219. https://doi.org/10.1002/eqe.2267.

Bathe, K.J. (2006), *Finite Element Procedures*, Prentice Hall, Pearson Education, Inc.

Bi, K., Hao, H. and Sun, Z. (2018), "3D FEM analysis of earthquake induced pounding responses between asymmetric buildings", *Earthq. Struct.*, **13**(4), 377-386. https://doi.org/10.12989/eas.2018.13.4.377.

Boo, S.H., Kim, J.H. and Lee, P.S. (2018), "Towards improving the enhanced Craig-Bampton method", *Comput. Struct.*, **196**, 63-75. https://doi.org/10.1016/j.compstruc.2017.10.017.

Chase, G.C., Boyer, F., Rodgers, G.W., Labrosse, G. and MacRae, A. (2014), "Probabilistic risk analysis of structural impact in seismic events for linear and nonlinear systems", *Earthq. Eng. Struct. Dyn.*, **43**, 1565-1580. https://doi.org/10.1002/eqe.2414.

Chau, K.T. and Wei, X.X. (2001), "Pounding of structures modelled as non-linear impacts of two oscillators", *Earthq. Eng. Struct. Dyn.*, **30**, 633-651. https://doi.org/10.1002/eqe.27.

Chau, K.T., Wei, X.X., Guo, X. and Shen, C.Y. (2003), "Experimental and theoretical simulations of seismic poundings between two adjacent structures", *Earthq. Eng. Struct. Dyn.*, **32**, 537-554. https://doi.org/10.1002/eqe.231.

Choi, C.K. and Lee, T.Y. (2003), "Efficient remedy for membrane locking of 4-node flat shell elements by non-conforming modes", *Comput. Meth. Appl. Mech. Eng.*, **192**, 1961-1971. https://doi.org/10.1016/S0045-7825(03)00203-2.

Chopra, A.K. (2007), *Dynamics of Structures, Theory and Applications to Earthquake Engineering*, Third Edition, Prentice Hall, New Jersey.

Craig, R.R. and Bampton, M.C. (1968), "Coupling of substructures for dynamic analyses", *AIAA J.*, **6**, 1313-1319. https://doi.org/10.2514/3.4741.

Davis, R.O. (1992), "Pounding of buildings modelled by an impact oscillator", *Earthq. Eng. Struct. Dyn.*, **16**, 253-274. https://doi.org/10.1002/eqe.4290210305.

Efraimiadou, S., Hatzigeorgiou, G.D. and Beskos, D.E. (2013), "Structural pounding between adjacent buildings subjected to strong ground motions. Part I: The effect of different structures arrangement", *Earthq. Eng. Struct. Dyn.*, **42**(10), 1509-1528. https://doi:10.1002/eqe.2285.

Efraimiadou, S., Hatzigeorgiou, G.D. and Beskos, D.E. (2013), "Structural pounding between adjacent buildings subjected to strong ground motions. Part II: The effect of multiple earthquakes", *Earthq. Eng. Struct. Dyn.*, **42**(10), 1529-1545. https://doi:10.1002/eqe.2284.

Ghandil, M. and Aldaikh, H. (2017), "Damage-based seismic planar pounding analysis of adjacent symmetric buildings considering inelastic structure-soil-structure interaction", *Earthq. Eng. Struct. Dyn.*, **46**, 1141-1159. https://doi.org/10.1002/eqe.2848.

Jankowski, R. (2005), "Non-linear viscoelastic modeling of earthquake-induced structural pounding", *Earthq. Eng. Struct. Dyn.*, **34**, 595-611. https://doi.org/10.1002/eqe.434.

Jankowski, R. (2006), "Analytical expression between the impact damping ratio and the coefficient of restitution in the non-linear viscoelastic model of structural pounding", *Earthq. Eng. Struct. Dyn.*, **35**, 517-524. https://doi.org/10.1002/eqe.537.

Jankowski, R. (2009), "Experimental study on earthquake-induced pounding between structural elements made of different building materials", *Earthq. Eng. Struct. Dyn.*, **39**, 343-354. https://doi.org/10.1002/eqe.941.

Jankowski, R. and Mahmoud, S. (2016), "Linking of adjacent three-story buildings for mitigation of structural pounding during earthquakes", *Bull. Earthq. Eng.*, **14**, 3075-3097. https://doi.org/10.1007/s10518-016-9946-z.

Kasai, K. and Maison, B.F. (1997), "Building pounding damage during the 1989 Loma Prieta earthquake", *Eng. Struct.*, **19**, 195-207. https://doi.org/10.1016/S0141-0296(96)00082-X.

Kheyroddin, A., Kioumarsi, M., Kioumarsi, B. and Faraei, A. (2018), "Effect of lateral structural systems of adjacent buildings on pounding force", *Earthq. Struct.*, **14**(3), 229-239. https://doi.org/10.12989/eas.2018.14.3.229.

Kim, J.H., Kim, J. and Lee, P.S. (2017), "Improving the accuracy of the dual Craig-Bampton method", *Comput. Struct.*, **191**, 22-32. https://doi.org/10.1016/j.compstruc.2017.05.010.

Komodromos, P. (2007), "Simulation of the earthquake-induced pounding of seismically isolated buildings", *Comput. Struct.*, **86**, 618-626. https://doi.org/10.1016/j.compstruc.2007.08.001.

Kun, C., Yang, Z. and Chouw, N. (2018), "Seismic response of skewed bridges including pounding effects", *Earthq. Struct.*, **14**(5), 467-476. https://doi.org/10.12989/eas.2018.14.5.467.

Laursen, T.A. (2003), *Computational Contact and Impact Mechanics*, Springer-Verlag Berlin Heidelberg.

Mavronicola, E. and Komodromos, P. (2011), "Assessing the suitability of equivalent linear elastic analysis of seismically isolated multi-storey buildings", *Comput. Struct.*, **89**, 1920-1931. https://doi.org/10.1016/j.compstruc.2011.05.010.

Muthukumar, S. and DesRoches, R. (2006), "A Hertz contact model with non-linear damping for pounding simulation", *Earthq. Eng. Struct. Dyn.*, **35**, 811-828. https://doi.org/10.1002/eqe.557.

Pantelides, C.P. and Ma, X. (1998), "Linear and nonlinear pounding of structural systems", *Comput. Struct.*, **66**, 79-92. https://doi.org/10.1016/S0045-7949(97)00045-X.

Rixen, D.J. (2004), "A dual Craig-Bampton method for dynamic substructuring", *J. Comput. Appl. Math.*, **168**, 383-391. https://doi.org/10.1016/j.cam.2003.12.014.

Shi J., Bamer F. and Markert B. (2018), "A structural pounding formulation using systematic modal truncation", *Shock Vib.*, **2018**, Article ID 6378085, 15. https://doi:10.1155/2018/6378085.

Tubaldi, E., Freddi, F. and Barbato, M. (2016), "Probabilistic seismic demand model for pounding risk assessment", *Earthq. Eng. Struct. Dyn.*, **45**, 1743-1758. https://doi.org/10.1002/eqe.2725.

Wriggers, P. (2006), *Computational Contact Mechanics*, Second Edition, Springer-Verlag Berlin Heidelberg.

Ye, K., Li, L. and Zhu, H. (2009), "A note on the Hertz contact model with nonlinear damping for pounding simulation", *Earthq. Eng. Struct. Dyn.*, **38**, 1135-1142. https://doi.org/10.1002/eqe.883.

Zargar, H., Ryan, K.L., Rawlinson, T.A. and Marshall, J.D. (2017), "Evaluation of a passive gap damper to control displacements in a shaking test of a seismically isolated three-story frame", *Earthq. Eng. Struct. Dyn.*, **46**, 51-71. https://doi.org/10.1002/eqe.2771.

Zhang, D., Jia, H., Zheng, S., Xie, W. and Pandey, M.D. (2014), "A highly efficient and accurate stochastic seismic analysis approach for structures under tridirectional nonstationary multiple excitations", *Comput. Struct.*, **145**, 23-35. https://doi.org/10.1016/j.compstruc.2014.07.017.

Zucca, S. and Epureanu, B.I. (2017), "Reduced order models for nonlinear dynamic analysis of structures with intermittent contacts", *J. Vib. Control*, **24**(12), 2591-2604. https://doi:10.1177/1077546316689214.

CC